



A Combined Modeling and Experimental Study Assessing the Impact of Fluid Pulsation on Charge and Energy Efficiency in Capacitive Deionization

Xia Shang,^{a,b} Roland D. Cusick,^{a,*} and Kyle C. Smith^{b,c,d,*}

^aDepartment of Civil and Environmental Engineering, University of Illinois at Urbana-Champaign, Urbana, Illinois 61801, USA

^bDepartment of Mechanical Science and Engineering, University of Illinois at Urbana-Champaign, Urbana, Illinois 61801, USA

^cBeckman Institute for Advanced Study, University of Illinois at Urbana-Champaign, Urbana, Illinois 61801, USA

^dComputational Science and Engineering Program, University of Illinois at Urbana-Champaign, Urbana, Illinois 61801, USA

Cell-cycling performance in capacitive deionization (CDI) can suffer from various charge-efficiency loss mechanisms. In conventional CDI, we show that salt residue within electrodes introduces a temporal lag between charge and desalination stages of a CDI cycle. Without accounting for this effect in the collection of effluent, significant performance degradation occurs as current density increases. To overcome this we use pulse-flow operation to control fresh- and brine-water concentrations. The charge and energy efficiency performance between the two flow-modes is compared using a porous electrode model that is calibrated and validated with experimental data. To quantify specific contributions to charge efficiency losses, the model captures local salt variations resulting from a combination of electrosorption, leakage current, and immobile surface charge. Compared to traditional continuous-flow operation, simulation results show that charge efficiency increases up to 23% in the pulse-flow operation at a current density up to 20 A/m², which leads to a 73% decrease of specific energy consumption (SEC). In addition, the SEC predicted by the pulse-flow operation model closely aligns with the predictions of the continuous-flow model after accounting for the temporal lag in effluent salinity. Both simulations and experimental results suggest that pulse-flow operation closely approximates the performance in continuous-flow operation.

© The Author(s) 2017. Published by ECS. This is an open access article distributed under the terms of the Creative Commons Attribution Non-Commercial No Derivatives 4.0 License (CC BY-NC-ND, <http://creativecommons.org/licenses/by-nc-nd/4.0/>), which permits non-commercial reuse, distribution, and reproduction in any medium, provided the original work is not changed in any way and is properly cited. For permission for commercial reuse, please email: oa@electrochem.org. [DOI: 10.1149/2.0841714jes] All rights reserved.



Manuscript submitted September 25, 2017; revised manuscript received November 2, 2017. Published December 8, 2017.

Capacitive deionization (CDI) is increasingly considered as an energy efficient technology for desalination of low salinity systems compared to reverse osmosis and thermal flash desalination.^{1–5} The electrosorption process in traditional CDI systems relies on conductive porous electrodes that undergo electrical double layer (EDL) charging when an external electric power source is applied.^{3,5–7} In CDI, charge efficiency⁸ is an important metric, defined as the moles of salt removed per mole of electronic charge transferred to a given electrode. Though theoretical CDI charge efficiencies can approach 100%, a number of factors reduce values observed in practice. Specifically, previous studies have shown that salt removal performance during CDI cell cycling can suffer from electrode degradation,^{9–11} parasitic side reactions,^{10–12} repulsion of co-ions during the electrosorption process,^{8,13,14} and low ion uptake capacity.^{15,16} In addition, CDI electrodes must operate at high current density to enable sufficient salt removal rates. In practice, there is a tradeoff between charge capacity and current.

On the other hand, salt adsorption capacity is affected by the charge storage capacity of CDI electrodes. Recent research has been conducted to improve electrosorption capacity by using high surface-area carbons (e.g., activated carbon,^{5,6} carbon aerogel,^{17,18} carbon nanotubes,^{19,20} graphene,^{21,22} and carbide derived carbon^{15,23}), metal oxides,²¹ surface-modified carbon,^{24–26} and sodium-ion intercalation materials.^{27–31} Activated carbon is the most common and widely studied material in CDI due to its low cost, abundance, and high surface area to promote electrosorption.^{5,6,16,23} However, the stability of activated carbon electrodes is limited by corrosion in aqueous solution in an oxidizing environment.^{11,32,33} Corrosion could lead to changes in surface chemistry and shifts of potential of zero charge (PZC).^{8,9,14,34,35} Such electrode properties have significant impact on desalination performance as they dictate the direction of the electrosorption process: charge accumulation can be driven either by the adsorption of ions

with sign opposite to the applied charge (counter-ions) or by repulsion of ions of the same sign (co-ions).^{8,13,25} On the other hand, immobile surface charge can be also engineered to improve stability and salt removal performance through surface group modification, such as acidification and amination, that leads to positive and negative shift of the electrode PZC, respectively.^{14,24,25,36–38}

Leakage current associated with parasitic side reactions, which is commonly observed during cycling tests of CDI cells, affects cell cycling in different ways.^{39–43} For example, the irreversible energy loss due to parasitic side reactions increases when CDI cells are cycled at low current density and with a large voltage window⁴⁴ (i.e., the difference between the terminal cell voltage in charge and discharge stages). Shift in the PZC of electrodes often occurs after long-term cycling due to parasitic faradaic reactions.⁴⁵ In addition, byproducts of side reactions (e.g., water splitting, oxygen reduction, and carbon corrosion) could introduce variations in local pH^{12,46} that can affect acid-base equilibria and influence electrosorption.⁴⁷ Shielding electrodes with a protective skin, such as ion exchange membranes, is a common method to prevent leakage current and improve system stability.^{34,45,48}

In addition to the aforementioned limitations, the impact of flow conditions on the desalination performance of CDI systems has only been explored to a limited extent. For a conventional flow-by CDI system that consists of a pair of porous electrodes and a spacer (Figure 1a), charge accumulation occurs at capacitive interfaces within nanoscopic micropores upon application of external current, according to the widely used Donnan based theory.^{15,49,50} As ions are removed from, or supplied to, micropores within a given electrode, salt concentration is modulated within larger scale pores, while transport of salt outside of the electrode region is driven by diffusion and migration.^{6,18,51} At high current density, as we will demonstrate with two-dimensional porous-electrode modeling, the spatial separation of electrode and flow-channel regions results in a lag of effluent salt concentration that reduces salt removal performance. Consequently, losses in charge efficiency during desalination can be attributed to

*Electrochemical Society Member.

[†]E-mail: rcusick@illinois.edu; kcsmith@illinois.edu

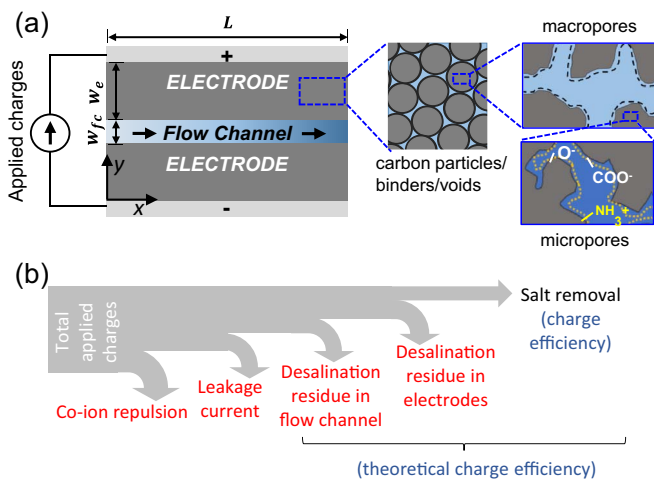


Figure 1. (a) Schematic of the simulated flow-by CDI cell. A uniform superficial velocity field advects solution through the flow channel with thickness w_{fc} and length L , while charge is transferred between electrodes of thickness w_e . Each electrode consists of activated carbon, polymeric binder, and void space. Activated carbon particles can be further divided into three regions: a solid carbon backbone that conducts electricity, a macropore region filled with electroneutral solution, and a micropore region where electrosorption takes place. The black dashed line represents the interface between macropores and micropores, and the yellow dashed lines represent Stern-layer interfaces. The immobile surface charges are treated as fixed charged groups that reside inside the micropores.^{25,52} (b) Schematic of the different pathways of charge utilization in the charge stage of a typical flow-by CDI cell. A fraction of externally applied charge is utilized for co-ion repulsion, leakage current, desalination residue in flow-channel, and desalination residue within electrode pores. The fraction of salt removal is based on the salinity difference between the influent and effluent, which is typically referred to as the charge efficiency.

a variety of effects (Figure 1b), including the following: (1) co-ion repulsion during electrosorption process, (2) leakage current due to parasitic side reactions, (3) desalination residue in the pore space of electrodes, (4) desalination residue in the flow channel, and (5) salt removal in the effluent.

Novel CDI flow architectures have been introduced using flow-through^{18,53} and fluidized-bed^{54,55} electrodes, but few studies have focused on understanding the role of flow conditions within flow-by CDI. In the context of electrochemical energy storage intermittent pulse-flow has been used to increase energy and coulombic efficiency in suspension-based flow batteries^{56–59} and flow capacitors,⁶⁰ but the impact of similar flow modes has not been explored in CDI. Continuous flow is most commonly used in CDI studies, in which influent solution is continuously pumped through the cell at a constant flow rate during cell cycling (as shown in Figure 2a).

Here, we compare the cycling of a flow-by CDI cell in pulse flow and continuous flow operation using a combination of porous electrode modeling and experimental demonstration. Computational models for the two operational schemes are developed, calibrated, and demonstrated with a self-designed CDI cell. We study cycling behavior under constant current operation, which recent work⁶¹ has demonstrated to be more energy efficient than constant voltage operation when energy recovery is included during the brine generation stage. Figure 2b shows a representative sequence of current and flow pulses applied during pulse-flow operation: (1) solution within electrodes remains stagnant until the average concentration in the flow channel reaches the fresh/brine concentration target, (2) a flow pulse is triggered to replace the solution in flow channel with a new batch of feed solution, and (3) this process is repeated until cell voltage reaches a pre-specified cutoff voltage. By controlling flow rate based on effluent concentration, the charge stage aligns with the desalination stage during pulse flow operation. In comparison, when continuous flow rate is used with the same average flow rate, a lag is observed between charge and desalination stages. We show here that specific

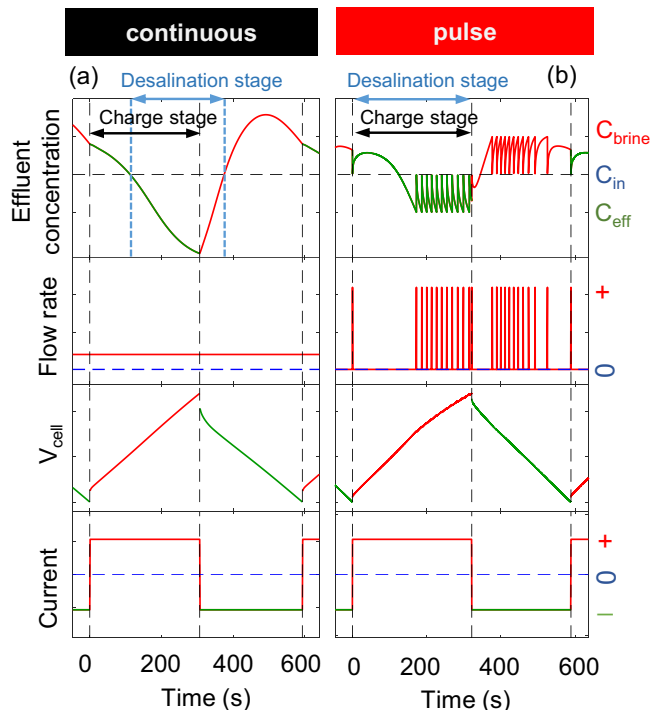


Figure 2. Schematic of (a) continuous-flow and (b) pulse-flow operation for a flow-by CDI cell. In the continuous-flow operation mode, the desalination stage lags behind the charge stage. In the pulse-flow mode the desalination stage and charge stage coincide.

energy consumption levels in continuous flow similar to pulse flow can be achieved by synchronizing effluent sampling based on real-time measurements of salinity.

Modelling

The porous electrodes used in the present CDI study are composed of three distinct regions: a solid region made of carbon, an electroneutral solution residing in so-called macropores, and a charge-accumulating region at solution/solid interfaces (i.e., micropores).^{15,49,50} The mass and charge transport processes in CDI occur over different length scales: the length of the cell L , the thickness of the electrode w_e , the radius of a single activated particle d_c , and the average radius of micropores $\langle r_{mi} \rangle$. For a CDI electrode made of activated carbon powder, the four characteristic length scales range from centimeters to atomic, with the following condition typically satisfied: $L \gg w_e \gg d_c \gg \langle r_{mi} \rangle$.

In the present porous electrode model, we incorporate microscopic electrosorption processes through an EDL model that includes the effects of salt concentration on the selective uptake of cations and anions. To define this model we first consider an activated carbon within the porous medium that is fully wetted with solution at rest. Solution in the macropores consists of positive and negative charged species that participate in the electrosorption process at the boundary of macropores and micropores. In the micropores, the electrosorption process (i.e., charge balancing through repulsion of co-ions or adsorption of counter-ions) takes place as a result of local electrical polarization $\phi_s - \phi_e$, where ϕ_s and ϕ_e are the solid potential and electrolyte potential, respectively. Here, we model the coupling between electrical polarization and stored charge with a Donnan-based theory where EDLs are highly overlapped.⁴⁹

We use Newman's macro-homogeneous porous electrode theory^{6,62} to model electron and ion transport through the extent of the electrodes and the flow channel. Here, the contributions of ionic migration and diffusion to the flux of individual species are accounted

for explicitly using the Nernst-Planck equations. Presently, we assume solution to be an electroneutral binary electrolyte, in which case the mass conservation equations for the two ionic species of interest (Na^+ and Cl^-) can be combined in such a way to produce an alternative but equivalent pair of governing equations: a potential-independent “salt conservation” equation and a current conservation equation.⁶³ Similar equations have been used in modeling transport in other desalination cells.^{18,27,62,64} The salt conservation equation in the electrode of a typical CDI cell in the absence of advection is:⁶

$$\frac{\partial \varepsilon_{ma} c}{\partial t} + \nabla \cdot (-D_{eff} \nabla c) = \dot{S}, \quad [1]$$

where ε_{ma} is the macroporosity that accounts for both macropore volume and voids among particles, c is local salt concentration, D_{eff} is the effective salt diffusivity that is calculated based on electrode porosity and bulk salt diffusivity D_0 as $D_{eff} = D_0 \varepsilon^{1.5}$,⁶⁵ and \dot{S} is a source/sink term that represents the rate of concentration change due to electrosorption and mass transfer. The amphoteric Donnan (amph-D) model^{25,66,67} is used to determine the source term, $\dot{S}(\phi_s - \phi_e, c) = -\frac{\varepsilon_{mi}}{F} \frac{\partial c_{ions,mi}}{\partial t}$, by accounting for the rate of salt adsorption, where ε_{mi} is the microporosity, F is Faraday's constant, and $c_{ions,mi}$ is the ionic concentration in micropores. The charge balance equation in micropores with surface immobile charge density ρ_{chem} is:

$$\rho_e + \rho_{mi} + \rho_{chem} = 0, \quad [2]$$

where ρ_e and ρ_{mi} represent the electronic and ionic charge densities, respectively. The electrode polarization in the amph-D model consists of a potential drop in the Stern layer $\Delta\phi_S$ and a Donnan potential $\Delta\phi_D$: $\phi_s - \phi_e = \Delta\phi_S + \Delta\phi_D$. Assuming the Stern layer capacitance is constant, $\Delta\phi_S$ and $\Delta\phi_D$ can be represented as $\Delta\phi_S = \frac{F \rho_e}{\rho_{electrode} C_S}$, and $\Delta\phi_D = -\text{arcsinh}(\frac{\rho_{mi}}{2c})$. The total ionic concentration in the micropores is given by:^{13,49}

$$(c_{ions,mi})^2 = (\rho_{mi})^2 + (2cF)^2, \quad [3]$$

Under the assumption of a symmetric electrolyte (ions with equal valence and equal diffusivity), current conservation can be expressed in terms of the electrostatic potential in solution ϕ_e as:

$$\nabla \cdot (-\kappa_{eff} \nabla \phi_e) = \varepsilon_{mi} \dot{Q} + i_L, \quad [4]$$

where $\dot{Q} = -\frac{\partial \rho_{mi}}{\partial t}$, and κ_{eff} is the local effective ionic-conductivity that depends on porosity ε and the corresponding bulk value κ_0 as $\kappa_{eff} = \kappa_0 \varepsilon^{1.5}$. The Nernst-Einstein relation is applied here to determine the value of local bulk ionic-conductivity $\kappa_0 = \frac{2D_0 c F e}{k_B T}$. Eq. 4 also includes leakage current per unit electrode volume i_L due to parasitic faradaic reactions on the electrodes. Note that the above governing equations are valid in either of the two contexts: (1) when parasitic reactions produce negligible amounts of charged species or (2) reaction rates are slow enough that the local solution composition (e.g., pH) is not perturbed by reactions. Otherwise, an asymmetric multi-species transport model based on Nernst-Planck equations is required to obtain accurate prediction of species-concentration distributions.¹²

Electronic conduction within solid materials (i.e., carbon network, current collector, and the external circuit) is assumed to follow Ohm's law $\nabla \cdot (-\sigma_{s,eff} \nabla \phi_e) = -\varepsilon_{mi} \dot{Q} - i_L$. Note that in conventional CDI simulation, the potential drop due to the solid phase resistance in the electrode is often ignored because the electronic conductivity of the carbon network, $\sigma_{s,eff}$, is typically much greater than κ_{eff} .^{44,51}

The salt conservation equation in the flow channel is governed by:

$$\varepsilon_{FC} \frac{\partial c}{\partial t} + \nabla \cdot (\vec{v}_s c) + \nabla \cdot (-D_{eff,FC} \nabla c) = 0, \quad [5]$$

where ε_{FC} is the porosity of the flow channel spacer, \vec{v}_s is the superficial velocity (assumed uniform), and $D_{eff,FC}$ is the effective salt diffusion coefficient in the flow channel. Since the direction of current is perpendicular to the direction of flow, a two-dimensional model is formulated for the continuous-flow operation scheme. In the model of pulse-flow operation, the effect of advection in Eqn. 5 can be neglected if we assume the event of pulsing happens instantaneously, as shown

in Ref. 56. This assumption simplifies the numerical implementation for pulse-flow operation model and yields a one-dimensional problem because variation along the direction of flow does not occur.

Boundary and initial conditions applied in the present model are described as follows. Ionic flux (excluding advective contributions) is set to zero at all surfaces except at the flow-channel inlet. When influent solution flows into the flow channel we impose a constant concentration boundary condition at the flow-channel inlet. In the absence of flow (for the one-dimensional model of pulse-flow operation) a null-flux condition is imposed at the flow-channel inlet. The total electronic current at the current collector surface of the positive/negative electrode is constrained to the total externally applied current, while the total ionic current is set to zero on these surfaces. In all simulations we initialize salt concentration across the entire cell to the chosen influent concentration, and charge density within the porous electrodes is initially set to zero. From these initial conditions initial cell voltage and ionic concentration inside micropores were calculated.

The voltage applied in CDI cycling is typically not high enough to induce reaction of water splitting. The faradaic side reactions we account for in the present model are carbon corrosion and oxygen reduction on the positive and negative electrodes, respectively.^{11,12,32,68} The dynamics of carbon corrosion in aqueous environment have been previously described with numerical models. We use Butler-Volmer kinetics to model these faradaic side reactions. On the positive electrode carbon corrosion occurs:^{32,69}

$$i_{L,+} = a^* i_{0,C} \theta e^{\left\{ \frac{\alpha_{C,a} F}{RT} (\phi_s - \phi_e - U_C^\theta) \right\}}. \quad [6]$$

On the negative electrode, oxygen reduction occurs:^{32,33,68,69}

$$i_{L,-} = -a^* i_{0,O_2} \left\{ e^{\frac{\alpha_{O_2,a} F}{RT} (\phi_s - \phi_e - U_{O_2}^\theta)} - \left(\frac{p_{O_2}}{p_{O_2}^*} \right)^{\beta_{O_2}} e^{\frac{-\alpha_{O_2,c} F}{RT} (\phi_s - \phi_e - U_{O_2}^\theta)} \right\}, \quad [7]$$

where $\phi_s - \phi_e$ is the local electrode polarization, $i_{0,i}$ is the exchange current density in A/m^2 (per unit of active surface area), a^* is the active surface area per unit volume of electrode, $\alpha_{i,a}$ and $\alpha_{i,c}$ are the transfer coefficients for the anodic and cathodic reactions, U_i^θ is the standard potential of carbon corrosion (positive electrode) and oxygen reduction (negative electrode), p_{O_2} is the partial pressure of O_2 , $p_{O_2}^*$ is the reference partial pressure of O_2 , and β_{O_2} is the concentration factor of O_2 . Here the empirical term,^{32,69} $\theta = \frac{e^{\left\{ \frac{F}{RT} (\phi_1 - \phi_2 - U_\theta) \right\}}}{1 + e^{\left\{ \frac{F}{RT} (\phi_1 - \phi_2 - U_\theta) \right\}}}$, is adopted

to improve model fitting in the low voltage polarization region (as discussed in the Model calibration and validation section and shown in the Supplementary Material). Leakage current sub-models were calibrated with experimental data. The reaction of carbon corrosion is considered irreversible and thus only the anodic reaction is used in the expression.^{32,69}

The modeling equations listed above lead to a coupled non-linear system that cannot be solved analytically. Numerical solutions were obtained by discretizing over the space and time domain using the finite-volume method.⁷⁰ The Crank-Nicolson method with a second-order central difference scheme was applied to diffusion flux and current terms, while an implicit method was used to integrate source terms with time. Electrode charge density variation with time was modelled using trapezoidal integration of local capacitive current. An algorithm was developed to solve the non-linear behavior wherein the self-consistent solution in the forward time step can be obtained with nested iteration loops. The concentration field was resolved in the inner loop, and the charge density and current distribution were solved in the outer loop. The numerical model was implemented in Matlab (The MathWorks, Inc.). The tolerance for a converged solution at a given time step was set at 10^{-7} mM and 10^{-6} C/cm³ for the iteration loops of concentration and charge density, respectively.

Experimental Setup and Methods

Flow cell design and setup.—The above model was implemented and validated based on a self-designed and built CDI cell that consists of two identical electrodes separated by a flow channel spacer with thickness of 250 μm . The electrode chamber on the graphite plate, as current collector (depth of 450 μm) was formed by surface etching with a 3D scanning and milling machine (Roland Modela MDX-20). A well-mixed carbon slurry, containing 90 dry-wt% activated carbon (AC) powder (Sigma-Aldrich) and 10 dry-wt% polyvinylidene fluoride (Sigma-Aldrich) in N-methyl-2-pyrrolidone (Alfa Aesar), was directly injected into the electrode chamber and stationed under vacuum at room temperature for 20 minutes to homogeneously fill the chamber and remove air bubbles. Then the graphite plate was placed on a hot plate at 70°C for 30 mins within a chemical fume hood to evaporate excess solvent, followed by immersion in deionized water for 24 hours to solidify the binder. The flow channel was cut out from a silicone gasket (SS-0.016-67909, AAA-Acme Rubber CO.), which was compressed by ca. 40% (estimated with a caliper) after assembling. A laser engraver (Epilog Legend Mini 24 Laser) was used to cut the gaskets and acrylic plates that sealed and held the cell together. A multi-channel potentiostat galvanostat (VMP3, Biologic) was used to provide and record electric signals in all flow cell testing.

Cell cycling procedure.—In all experiments electrodes were freshly prepared at the beginning of each experiment with an electrode mass of $21 \pm 1 \text{ mg/cm}^2$ (sample-to-sample mass varied largely due to the repeatability of the electrode casting procedure used). The same electrodes were used for the set of validation tests at four different current densities, while the results in Figs. 4 and 5 were obtained with a different set of electrodes. In order to characterize cycling response for a limiting charge/discharge cycle, the cell was cycled under constant current for more than 30 cycles before limit-cycle data was collected. To further characterize electrode degradation capacitance was measured before and after experiments, where it was found that capacitance decreased by less than 10%.

All flow cell cycling experiments were performed at constant current with an influent NaCl solution at 30 mM. Initially, the flow cell with uncharged electrodes was set to an open circuit condition (OCC), while being simultaneously rinsed with influent solution overnight to reach equilibrium. By applying a constant current density, the charge stage commenced until cell voltage reached its terminal value (1.2 V), after which the direction of current was reversed to induce discharge of the cell. The next charge cycle with the same settings of current density and voltage limit began after V_{cell} decreased to 0 V. In all cases charge/discharge cycles were performed until a limit cycle was reached in which an asymptotic response was observed, such that the difference between the voltage profiles of two consecutive charging cycles was negligible.

In continuous-flow operation, the flow rate, determined based on the average flow rate in the pulse-flow operation under the same testing condition, was maintained constant throughout the cycling experiment. A syringe pump (PHD 2000, Harvard Apparatus) was used in order to reduce fluctuations in flow rate. The conductivity in the effluent was continuously measured and recorded using a flow-through conductivity sensor that has an internal volume of 93 μL (ET908, EDAQ).

During pulse-flow cycling a programmable peristaltic pump (Masterflex) was used to advance solution through the flow channel. Here, a fixed volume of influent solution was pumped at a high flow rate (Q_{pulse}) of 0.7375 mL/s for 1.2 s. To implement the pulse-flow strategy and the cycling tests in a synchronized way, one channel of the potentiostat was used to provide analog signals for pump control. In order to minimize the effect of dispersion and mixing in the dead volume of the system (e.g., volume of adaptors and tube fittings), the volume dispensed in a pulse (V_{pulse}) was about twice the volume of the open space in the flow channel (V_{FC}). When the system reached a limit cycle, a small vial was used to collect effluent of every one or two pulses for further analysis, depending on whether it was the last

pulse in the charge/discharge stage. The conductivity of the effluent samples was measured immediately after the cycling test with a dip-in micro-conductivity probe (InLab 751, Mettler Toledo). The total salt removal/generation was determined based on the total volume of dispensed solution and the difference in salinity between the influent and effluent water samples.

Leakage current test.—The leakage current due to parasitic reactions was characterized using a setup similar to that of desalination cycling tests (see Figure S1 in the Supplementary Material). In these experiments, testing solution was continuously pumped through the CDI flow cell and cell voltage was incrementally increased by 0.1 V from 0 – 1.2 V for a duration of 2 hours every step to ensure completion of the electrosorption process.⁷¹ The current toward the end of every voltage step was recorded as the leakage current. Meanwhile, the potential of both electrodes was measured with Ag/AgCl reference electrodes placed next to the corresponding graphite plate via a salt bridge filled with the same testing solution. The solution in the feed tank was sparged with filtered air or nitrogen gas to evaluate the impact of dissolved oxygen on parasitic faradaic reactions of activated carbon electrodes in aqueous environment. In addition, another comparison experiment was performed after covering the positive and negative electrode with an anion exchange membrane (FUJIFILM) and a cation exchange membrane (FUJIFILM), respectively. Such a cell arrangement, commonly referred to as membrane capacitive deionization (MCDI), was used to confirm that transport of dissolved oxygen from the flow channel to the electrode, which was blocked under the presence of ion exchange membranes, played an important role in the faradaic reaction process (Figure S3).

Model Calibration and Validation

We calibrated and validated the present porous electrode model using independent experiments. The present model contains many parameters (see Table I), the majority of which were determined from independent experiments or were assumed based on prior literature. Four of these parameters were calibrated to obtain fits between simulated and experimental cycling data (Figure 3): Stern-layer capacitance (C_s), immobile surface charge density on the positive electrode (ρ_{chem}), exchange current density for oxygen reduction (i_{0,O_2}), and effective surface area for faradaic reactions (a^*). With these fitted parameters independent experiments at other operating conditions were used to validate the model in pulse-flow operation and continuous-flow operation (Figure 4).

Calibration of Stern-layer, immobile charge, and kinetic parameters.—Calibration was performed by sequentially adjusting individual model parameters. First, a^* was determined by fitting Eq. 6 to the experimental results from the leakage current test for the positive electrode using the linear least squares method (as shown in Figure 3a).⁷² Note that if the adsorption term θ in Eq. 6 is omitted a classical Butler-Volmer equation results, and the fitted model would deviate from the experimental observation slightly as it over estimated the leakage current at low voltage region (see Figure S2 in the Supplementary Material). By assuming that the value of a^* in the positive and negative electrodes is the same (since both electrodes were fabricated with the same recipe), we can obtain the value of i_{0,O_2} by fitting Eq. 7 to the leakage current testing result for the negative electrode (Figure 3b).

After incorporating a^* and i_{0,O_2} into the model, cell cycling experiments and simulations were performed at 6 A/cm² in the pulse-flow operation with a fixed batch time of 40 s (38.8 s of pump off and 1.2 s of pump on). As effluent salinity was not continuous in time during pulse-flow operation, we define two desalination metrics for pulse-flow operation based on the number of pulses in a limit cycle. The cumulative salt removal is defined as the sum of salt removed/generated through pulsing since the first pulse in the charge

Table I. Key modeling parameters.

Description	Symbol	Value	Unit	Note
<i>Cell design and testing parameter</i>				
Temperature	T	298.16	K	
Electrode density	$\rho_{electrode}$	0.4664	g/cm ³	
Transference number of cations	t_+	0.5		
Porosity of spacer	ε_{FC}	0.7		
Projected surface area	A_{ele}	18	cm ²	
Thickness of the positive electrode	$W_{e,pos}$	450	μm	
Thickness of the negative electrode	$W_{e,neg}$	450	μm	
Thickness of flow channel	W_{fc}	250	μm	
Resistance of current collector, contact resistance, wires, and power supply		0.5	Ω	
Diffusion coefficient of NaCl in dilute environment	D_0	1.61×10^{-5}	cm ² /s	
Effective electronic conductivity	$\sigma_{s,eff}$	7.57	S/m	
<i>Electrosorption model parameters</i>				
Stern layer capacitance	C_S	49	F/g	*
Macro-porosity of electrode	ε_{macro}	0.35		
Micro-porosity of electrode	ε_{micro}	0.25		
Charge density on positive electrode	ρ_{chem}	4	C/cm ³	*
<i>Faradaic reaction parameters</i>				
Oxygen reduction exchange current	i_{0,O_2}	5.5×10^{-6}	A/m ²	*
Henry's constant of oxygen	H_{O_2}	0.032		
Oxygen reduction potential at pH 7	$U_{O_2}^0$	0.81	V vs. SHE	
Symmetry factor for oxygen reaction	α_{O_2}	0.5		
Carbon oxidation exchange current	$i_{0,C}$	2.5×10^{-10}	A/cm ²	32,68
Carbon oxidation standard potential	U_C^0	0.207	V vs. SHE	32,68
Symmetry factor for carbon reaction	α_C	0.5		
Active surface area for faradaic reaction	a^*	1.1	m ² /cm ³	*
Langmuir adsorption potential	U_θ	1	V vs. SHE	32,68

*Fitting parameters.

stage as:

$$\sum(\Gamma) = \sum_1^N \Gamma_i \quad [8]$$

where Γ_i represents the moles of salt removed in pulse number i , which is calculated based on the difference between influent concentration (c_0) and concentration of the effluent collected from that pulse ($c_{out,i}$): $\Gamma_i = (c_0 - c_{out,i})V_{pulse}$. N is the number of flow pulses used.

The cumulative energy input is calculated based on the cell voltage in the charge stage of a limit cycle:

$$\sum(E) = \int_{t_0}^{t_i} V_{cell}(t) I dt \quad [9]$$

where t_0 and t_i represents the time at the start of charge stage and the time at the end of pulse number i , respectively.

Even though the electrodes were freshly prepared prior to experiments, the stability of electrodes changed during cell cycling, which has been commonly observed in conventional flow-by CDI system.^{9,14,24,38,73} This electrode degradation effect, resulting in gradual decrease in salt adsorption capacity, is mainly due to shift of the PZC of positive electrode as parasitic reactions (such as carbon corrosion) introduce changes in the immobile charges (ρ_{chem}) to the electrode surface. Previous work reported an increase of the equilibrium potential of the positive electrode by ca. 500 mV, while the PZC of the negative electrode remained almost the same after 50 charge/discharge cycles in a flow-by CDI cell.⁴⁵ Therefore, in the present model, we assume that changes in ρ_{chem} only occur on the positive electrode due to parasitic reaction of carbon corrosion. Furthermore, we set the value of ρ_{chem} for both the acidic and alkaline groups of the pristine electrode to zero in order to reduce the total number of fitting parameters. Note that this assumption yields the same equations of a Donnan based theory used in Ref. 67, which is also an extreme case in the amph-D theory^{25,66} in which the chemical charge density of the positive and negative regions of un-treated electrodes are 0 C/cm³.

Figures 3c, 3d show the experimental results obtained in the charge stage of a limit cycle for pulse-flow operation in order to extract the values of C_S and ρ_{chem} . Since the effect of these two parameters is

coupled within the model, we first set ρ_{chem} to 0 C/cm³ and tuned the value of C_S in model predictions until a good fit was obtained (Figure 3c), wherein the sum of squared differences in $\sum(E)$ between model prediction and experimental measurement was minimized. Next, we fixed the value of C_S and tested the sensitivity of ρ_{chem} from 0 C/cm³ to 10 C/cm³ to determine the optimum value of ρ_{chem} based on the

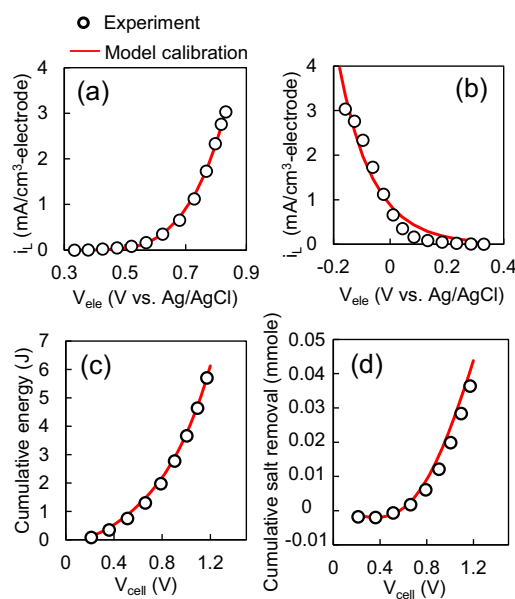


Figure 3. Model calibration. Experimental results in the leakage current tests and model fitting of leakage current density as a function of electrode voltage for the (a) positive and (b) negative electrodes. Experimental results from a limit cycle in the pulse-flow CDI operation at 6 A/cm² and model fitting for (c) cumulative salt removal and (d) cumulative energy in the charge stage.

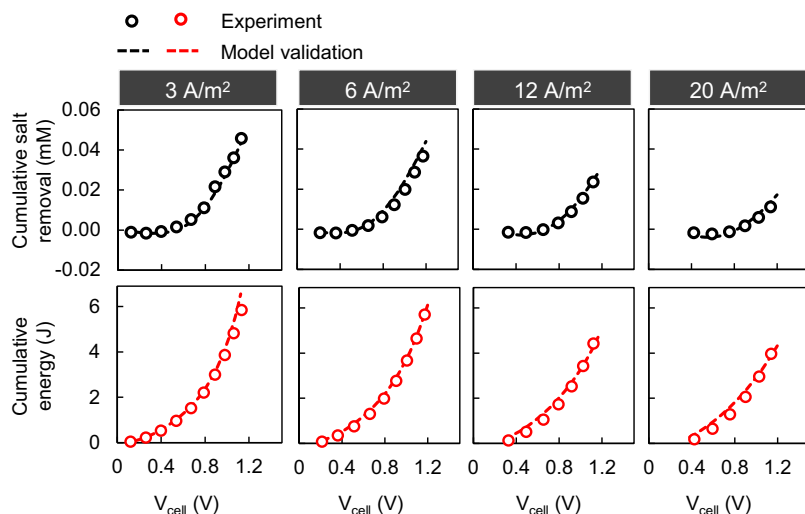


Figure 4. Model validation for pulse-flow operation. Cumulative salt removal (top row) and energy input (bottom row) for a number of pulses during the charge stage of pulse-flow operation at current densities from 3 A/m² to 20 A/m². The testing case at 6 A/m² was used as model calibration.

profile of $\sum(\Gamma)$ (Figure 3d and Figure S4a in the Supplementary Material). These two steps were iterated upon to produce adequate model fitting, as adjustments of ρ_{chem} affect $\sum(E)$ on a relatively small scale (see Figure S4b in the Supplementary Material). In summary, the values of all the fitting parameters were determined as follows: $C_S = 49$ F/g, $\rho_{chem} = 4$ C/cm³-electrode, $i_{0,O_2} = 5.5 \times 10^{-6}$ A/m², and $a^* = 1.1$ m²/cm³-electrode. All simulation results presented in following sections are based on these four values. We note that the fitted value of i_{0,O_2} may be biased by the value for $i_{0,C}$ assumed from the literature.

Validation of pulse-flow operation.—Salt removal and energy consumption for the present CDI device were found to vary with applied current density. Here tests in pulse-flow operation were conducted with current densities of 3 A/m², 6 A/m², 12 A/m², and 20 A/m² and constant batch times of 80 s, 40 s, 20 s, and 12 s, respectively. As shown in Figure 4, both $\sum(\Gamma)$ and $\sum(E)$ decreased significantly at high current densities. The model predictions aligned well with the evolution of $\sum(\Gamma)$ and $\sum(E)$ measured in experiment for the charge stage of a limit cycle.

Validation of continuous-flow operation.—The continuous-flow operation model was validated under the same current densities as that in pulse-flow operation, in which the total number of pulses occurred in the charge stage was used to determine the equivalent flow rate applied in the continuous-flow operation test at the same

current density. Model prediction and experimental data for effluent concentration and cell voltage are shown in Figure 5. Compared to the cumulative metrics applied in pulse-flow operation, effluent concentration and cell voltage are used here because: (1) they preserve the most representative information of the system as they were obtained directly in the experiment without further processing, and (2) small discrepancy between the model and experimental results are easily distinguished.

The continuous-flow operation model accurately predicted the cell voltage (bottom row in Figure 5) and captured the trend of effluent concentration (top row in Figure 5). However, a discrepancy between model prediction (plotted in solid red lines) and experimental data (plotted in solid black lines) is evident in the profiles of effluent concentration. We attribute this discrepancy mainly to the effect of mixing within the dead-volume (0.46 mL) between the end of desalination flow channel (0.34 mL) and the conductivity sensor in the experimental setup (see Figure S5 in the Supplementary Material). To corroborate this idea, we also modeled the dead-volume as a simple well-mixed reactor taking the effluent from the flow channel as influent to the tank,⁵³ the details of which are described in the Supplementary Material. The results after considering this effect of mixing are plotted in dashed red lines in Figure 5. Agreement between model and experiment improved when accounting for this effect, but the effect of mixing is hereafter omitted from subsequent results because: (1) the dead-volume should be minimized in a better designed cell, and (2) neglecting mixing enables direct comparison between the continuous- and pulse-flow operation modeling results.

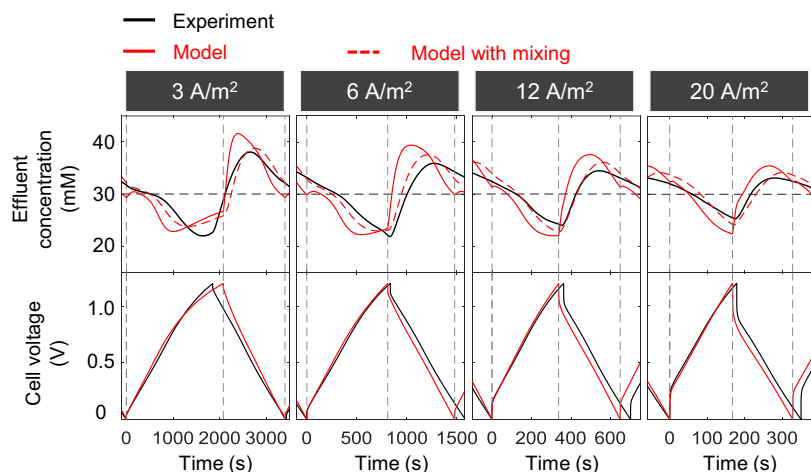


Figure 5. Model validation for continuous-flow operation at different current densities. Top row: effluent concentration as a function of time during a limit cycle. The red dashed lines are the simulated effluent concentration after accounting for the effect of mixing in the dead volume (e.g., adaptor and tube fitting) between the conductivity sensor. Bottom row: experimental and simulated results of cell voltage as a function of time in a limit cycle.

Results and Discussion: Comparison Between Pulse- and Continuous-Flow Operation

We now analyze the desalination performance of pulse- and continuous-flow modes using the calibrated and validated porous electrode model, after which we compare performance for these modes from experimental data. The overall system performance was evaluated by calculating the salt specific energy consumption for three conditions: (1) pulse-flow operation, (2) continuous-flow operation, and (3) continuous-flow operation accounting for the temporal displacement between the desalination stage and charge stage. Subsequently, we quantify the contributions of different sources of loss to charge efficiency. The spatiotemporal variation of concentration, charge density, and voltage are presented to identify charge-efficiency loss mechanisms. Finally, we report experimental data for a self-designed CDI cell and demonstrate that pulse-flow operation is a promising alternative to continuous-flow operation in CDI cycling.

Specific energy consumption of salt removal.—The specific energy consumption (*SEC*) of salt removal was chosen to evaluate the overall desalination performance for a limit cycle of a CDI cell. *SEC* for the three testing conditions was calculated as:

$$SEC_{pf} = \frac{\sum(E)}{M_{NaCl} \sum(\Gamma)} \quad \text{for pulse-flow operation,} \quad [10]$$

$$SEC_c = \frac{\int_{t_{SC}}^{t_{SD}} V_{cell} I dt}{M_{NaCl} \int_{t_{SC}}^{t_{SD}} (C_0 - C_{eff}) Q dt} \quad \text{for continuous-flow operation, and} \quad [11]$$

$$SEC_{c, \text{displace}} = \frac{\int_{t_{SC}}^{t_{SD}} V_{cell} I dt}{M_{NaCl} \int_{t_0}^{t_1} (C_0 - C_{eff}) Q dt} \quad \text{for continuous-flow operation with displacement.} \quad [12]$$

Here $\sum(E)$ and $\sum(\Gamma)$ represent the cumulative energy and salt removal in the pulse-flow operation, respectively. M_{NaCl} is the molecular weight of sodium chloride. V_{cell} is the cell voltage. Q is the flow rate in the continuous-flow operation. t_{SC}/t_{SD} represents the starting time for the charge/discharge stage. t_0/t_1 represents the time at the start/end of desalination stage (see Figure 2a).

The *SEC* of the two operating schemes was measured with a range of current densities from 2.2 A/m² to 20 A/m², as shown in Figure 6. Assuming 100% charge efficiency these current densities correspond to salt removal rates between 0.023 mmol/m²-s and 0.21 mmol/m²-s. The pulse-flow and continuous operation behave similarly at low current density region (i.e., less than 6 A/m²) but the two curves deviate significantly with increasing current density. For example, by increasing the current density from 6 A/m² to 18 A/m², a six-fold increase in *SEC* was observed in continuous-flow operation while the *SEC* of pulse-flow operation only increased by 50%. Note

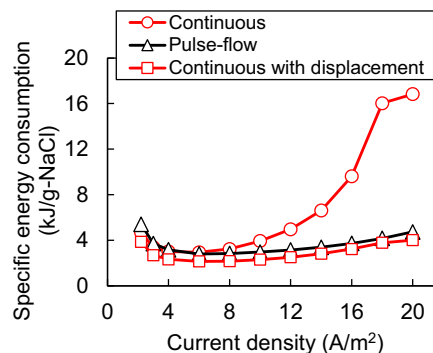


Figure 6. Simulation results of specific energy consumption of salt removal for pulse-flow operation and continuous-flow operation at current densities of 2.2–20 A/m² and with $C_0 = 30$ mM and $C_{eff} = 20$ mM.

that the production rate (i.e., total volume of solution treated in the charge stage) of the two operation modes was almost the same in the simulation (see the Experimental setup and methods section).

The effect of temporal displacement between the desalination stage and the charge stage in continuous-flow operation plays an important role in calculating the total salt removal within a limit cycle for constant current operation. After considering this effect, the *SEC* of continuous-flow operation dropped substantially, especially at high current densities (i.e., greater than 10 A/m²). We also observed that the *SEC* of the pulse-flow operation is located very close to the *SEC* of continuous-flow operation after accounting for the effect of displacement. This effect indicates that the pulse-flow 1-D model can be used to predict the system performance during continuous-flow operation.

In addition to *SEC* we calculated the average effluent salinity and salt removal rate for current densities toward the low and high ends of the tested range (Table II). At 6 A/m², pulse- and continuous flow perform similarly in terms of effluent salinity, salt removal capacity, water production rate, and salt removal rate. At 16 A/m² average effluent salinity in continuous-flow increases to 26.3 mM, resulting in low salt removal (3.94 mmol/cm²), high *SEC* (9.61 kJ/g-NaCl), and low salt removal rate (0.019 mmol/m²-s) in comparison with pulse-flow and continuous-flow with displacement.

Charge efficiency loss mechanisms.—Here we analyze the sources of loss in charge efficiency for the two operation schemes of interest. The total electrical charge (including both positive and negative charges), Q_T , applied to a given electrode during the charge stage is:

$$Q_T = 2I(t_{SD} - t_{SC}). \quad [13]$$

Utilization of applied charge for salt removal in a CDI system can be characterized into five distinct pathways denoted as follows: co-ion

Table II. Comparison of salt removal metrics between pulse- and continuous flow operation. The results are based on simulation at constant currents of 6 A/m² and 16 A/m² in the charging stage (desalination stage for the continuous-flow with displacement condition) within a limiting cycle.

Flow mode	Current density A/m ²	Salt removal mmol/cm ²	Produced water in a single cycle L/m ²	Avg. effluent salinity mM	Salt removal rate* mmol/m ² /s	SEC kJ/g-NaCl
Pulse-flow	6	20.4	2.10	20.3	0.025	2.80
Continuous	6	19.0	2.11	21.0	0.024	2.94
Continuous with displacement	6	22.6	1.83	17.7	0.033	2.47
Pulse-flow	16	11.9	1.23	20.3	0.053	3.72
Continuous	16	3.94	1.06	26.3	0.019	9.61
Continuous with displacement	16	10.0	0.90	18.9	0.057	3.76

*The salt removal rates in pulse-flow and continuous-flow operation are based on the length of charging stage. In continuous-flow operation with displacement, the length of the desalination stage is used to calculate the salt removal rate.

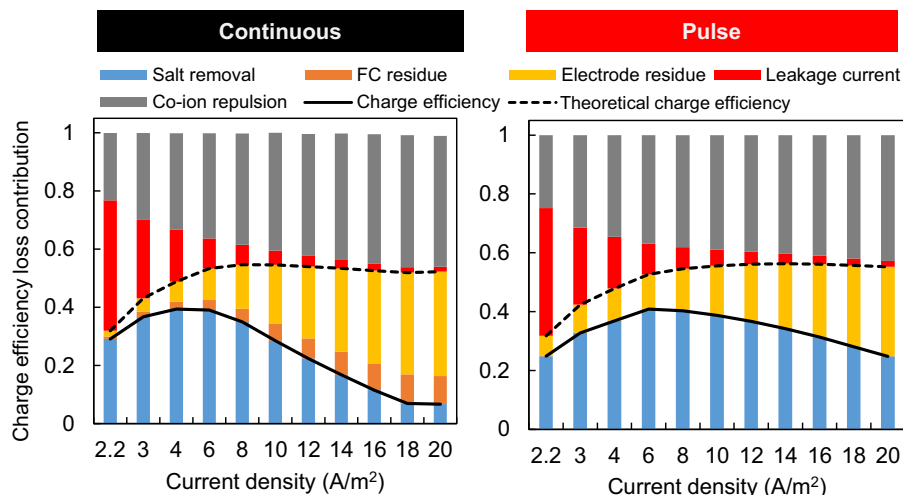


Figure 7. Simulation results for the contributions to charge efficiency for pulse-flow operation and continuous-flow operation in the charge stage of a limit cycle at current densities between 2.2–20 A/m² and with $C_0 = 30$ mM. The charge efficiency and theoretical charge efficiency are outlined using solid and dashed lines, respectively.

repulsion during electrosorption process (co-ion), leakage current due to parasitic faradaic reactions (leakage), observed salt removal in the effluent (salt), desalination residue in the flow channel (FC-res), and desalination residue in the macropores of electrodes (ele-res). Note that, for a CDI system operated under constant voltage, the contributions from the latter two mechanisms can be negligible if the cell reaches a uniform equilibrium concentration of C_0 toward the end of charge/discharge stage.^{5,18,23,52} The charge efficiency of each process (Λ_i) can be calculated as the ratio of total changes in electronic or ionic charge associated with that process to Q_T :

$$\Lambda_{salt} = \frac{2F \int_{t_{SC}}^{t_{SD}} (C_0 - C_{eff}) Q dt}{Q_T} \text{ for salt removal,} \quad [14]$$

$$\Lambda_{co-ion} = \frac{(\sum |Q_{mi,t_{SD}}| - \sum W_{mi,t_{SD}}) - (\sum |Q_{mi,t_{SC}}| - \sum W_{mi,t_{SC}})}{Q_T}$$

$$\text{for co-ion repulsion,} \quad [15]$$

$$\Lambda_{leakage} = \frac{\int_{t_{SC}}^{t_{SD}} (f i_L dV_{electrode}) dt}{Q_T} \text{ for leakage current,} \quad [16]$$

$$\Lambda_{FC-res} = \frac{(\oint c_{t_{SC}} dV_{FC} - \oint c_{t_{SD}} dV_{FC}) 2F}{Q_T} \text{ for flow-channel residue, and} \quad [17]$$

$$\Lambda_{ele-res} = \frac{(\oint c_{t_{SC}} dV_{electrode} - \oint c_{t_{SD}} dV_{electrode}) 2F \epsilon_{macro}}{Q_T} \text{ for flow-channel residue,} \quad [18]$$

where $\sum Q_{mi,t_i}$ and $\sum W_{mi,t_i}$ are the total number of charges and ions (both expressed in coulombs) in the micropores of both electrodes at time instant t_i . These quantities are expressed as $\sum Q_{mi,t_i} = \epsilon_{micro} \times \oint \rho_{mi,t_i} dV_{electrode}$, and $\sum W_{mi,t_i} = \epsilon_{micro} \times \oint c_{ions,mi,t_i} dV_{electrode}$. Note that, from the standpoint of charge conservation at the cell level, the component-wise calculation of charge efficiency also serves as a metric to quantify the computational error (ϵ) in the simulation, represented as $\epsilon = 1 - \sum \Lambda_i$. Here, we find ϵ to be less than 0.1% in all cases.

The simulation results of individual charge efficiency as a function of current density for the continuous- and pulse-flow operation modes are summarized in Figure 7. Similar monotonic changes in co-ion repulsion and leakage current are observed for both operation schemes: leakage current consumed the largest percentage of total charge (44.8% in continuous-flow operation and 43.4% in pulse-flow

operation) at the lower end of tested current density (2.2 A/m²), and the effect of co-ion repulsion dominated the usage of total charge (45.0% in continuous operation and 42.8% in pulse-flow operation) at the higher end of tested current density (20 A/m²). This trend agrees with previous studies on energy breakdown of a CDI cell operated under constant current mode.⁴⁴

Theoretical charge efficiency indicates the total capacity of salt removal that a given CDI system could achieve without changing the electrode composition, cell architecture, and operation scheme. In the present models, it was calculated as the sum of Λ_{salt} , Λ_{FC-res} , and $\Lambda_{ele-res}$. The charge efficiency due to salt removal in the effluent Λ_{salt} is highlighted in the figure using a black solid line. Both operation schemes showed similar theoretical charge efficiency, which gradually increased with current density and exhibited a plateau of 52% in the continuous-flow operation and 55% in the pulse-flow operation. The charge efficiency first increased with current density to a maximum value at around 6 A/m² and then decreased. In pulse-flow operation, the charge efficiency dropped to 25% at 20 A/m², however the charge efficiency of the continuous-flow operation at such current density decreased to a minimum of 7%.

To compare the sources of loss in charge efficiency, the difference of individual charge efficiency loss between the pulse-flow operation and continuous-flow operation are plotted in Figure 8. It appears that, in the high current density region (e.g., greater than 8 A/m²), the desalination residue in the flow channel and electrode are the two leading mechanisms, followed by the effect of co-ion repulsion, that favor the salt removal performance in pulse-flow operation compared to continuous-flow operation. For example, contributions from Λ_{FC} and Λ_{ele} consumed additional 10.2% and 7.3% of the total applied charge in continuous-flow operation compared to pulse-flow

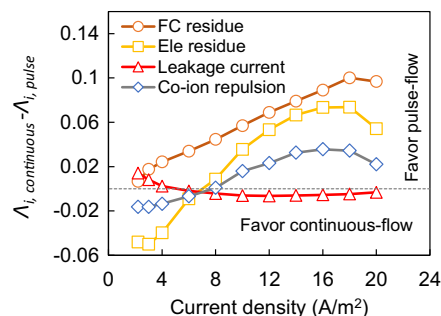


Figure 8. Difference in charge efficiency loss between pulse-flow operation and continuous-flow operation for the four loss mechanisms to charge efficiency: desalination residue in flow channel, desalination residue in electrode, leakage current, and co-ion repulsion.

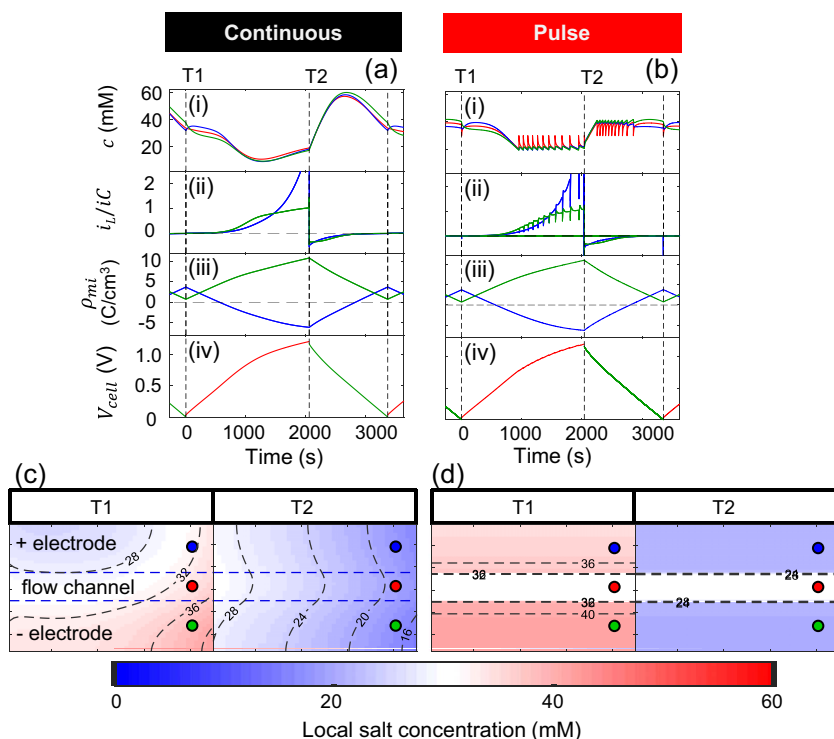


Figure 9. Time evolution of (i) salt concentration, (ii) leakage current (normalized by the capacitive current), (iii) ionic charge density within micropores, and (iv) cell voltage in a limit charge/discharge cycle at low current density of 3 A/m^2 for (a) continuous- and (b) pulse-flow operation modes. Two-dimensional contour plots show the distribution of salt concentration at time instant T1 (start of charge stage) and T2 (start of discharge stage) for (c) continuous- and (d) pulse-flow operation. The color scheme in (i-iii) corresponds to the three colored dots located in the contour plots.

operation at a current density of 18 A/m^2 . This finding indicates that minimizing the volume of free space (i.e., flow channel and void-space of electrodes) can lead to more efficient desalination of CDI.

Spatial distribution of salinity and charge density.—In the previous sections, we have compared the desalination performance between the pulse- and continuous-flow operation modes based on cumulative metrics including *SEC* and current efficiency. The two-dimensional distribution of salinity and charge density are discussed in this section to show the direct impact of different charge utilization mechanisms on salt removal.

The positive and negative electrodes in the present model are symmetrically arranged. However, they perform asymmetrically due to different settings on immobile surface charge density and faradaic reactions (see Eqs. 6–7 and the Model calibration and validation section). Here we selected three points inside the cell, indicated using blue (located at $x = 0.9L$, $y = 1.5w_e + w_{fc}$), red (located at $x = 0.9L$, $y = w_e + 0.5w_{fc}$), and green (located at $x = 0.9L$, $y = 0.5w_e$) circles on the color maps in Figures 9 and 10 to show the evolution of c , the ratio of leakage current to capacitive current (i_L/i_C), and ρ_{mi} at 3 A/m^2 (Figures 9a–9c) and 18 A/m^2 (Figures 10a–10c). Note that the blue and green points, located in the positive and negative electrode respectively, are symmetric with respect to the red point, which resides on the center line of the flow channel. The spatial distribution of local concentration at time instants T1 (start of charge stage) and T2 (start of discharge stage) are shown in two-dimensional contour plots.

At low current density, no distinct differences are observed between the evolution of local concentration among the two cases (Figure 9ai), indicating a small degree of concentration polarization. The local concentration during continuous-flow operation reached a minimum in the charge stage at a time when the development of cell voltage also deviated from the original trajectory (Figure 9aiv). This effect occurs because leakage current consumes more current than the capacitive current when operating at low current density and as cell voltage increases (Figure 9aiv). This effect also leads to sluggish electrosorption as the development of micropore charge density slows

down (Figure 9aiv). Similar trends of leakage current, charge density, and cell voltage are observed during pulse-flow operation (Figure 9bii–9biv)). Despite these similarities, local concentration variations are less extreme for pulse-flow (ca. 20 mM – 40 mM , see Figure 9bi), as a result of the target concentration of product and brine solution being pre-defined. This finding indicates that better control of effluent salinity can be achieved in pulse-flow operation.

An inversion of salt electrosorption, defined as desorption in the charge stage and adsorption in the discharge stage, is evident on the positive electrode at the beginning of the charge stage and toward the end of the discharge stage (Figure 9i–9ii). The degree of inversion, quantified by the micropore charge density on the positive electrode, dropped by 31% at T1 when current density increased from 3 A/m^2 ($\rho_{mi, pos} = 3.77 \text{ C/cm}^3$ – electrode) to 18 A/m^2 ($\rho_{mi, pos} = 2.61 \text{ C/cm}^3$ – electrode). However, the charge efficiency loss due to co-ion repulsion, which increases as a result of electrosorption inversion, is the dominant mechanism at high current density (see, also, Figure 7). The effect of inversion on charge efficiency is exacerbated at high current because of the pronounced cell polarization due to ohmic drop.^{74,75} Polarization at high current decreases the achievable charge utilization within the defined cell voltage window. As a result, the inversion process occurs over a larger fraction of the total cycle time at high current (Figure 10iii).

Concentration polarization between the flow channel and electrode is more pronounced (Figure 10a–10bi and Figure 10c–10d) as current density increases, resulting in further decrease in desalination performance due to desalination residue in the electrodes. In addition, the impact of leakage current on charge efficiency is negligible at high current density as the coulombic efficiency is close to unity (i.e., the coulombs removed during discharge balance with those supplied during charge).

Pulse-flow operation modeling results reveal that concentration polarization along the direction of flow (longitudinal) is absent during such a flow scenario (as shown in the salinity maps in Figures 9–10). However, during continuous-flow operation, the limitation of the longitudinal concentration polarization on salt removal performance increases with current density as large local concentration gradient develop. Such sharp concentration gradients could

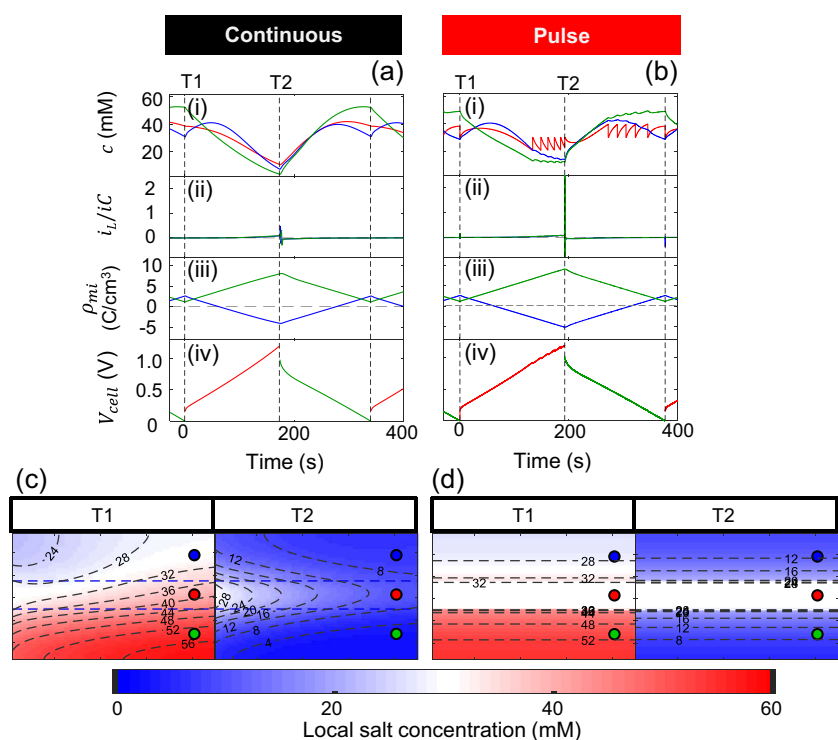


Figure 10. Time evolution of (i) salt concentration, (ii) leakage current (normalized by the capacitive current), (iii) ionic charge density in micropores, and (iv) cell voltage in a limit charge/discharge cycle at high current density of 18 A/m^2 for (a) continuous- and (b) pulse-flow operation modes. The two-dimensional contour plots show the distribution of local concentration at time instant T1 (start of charge stage) and T2 (start of discharge stage) for (c) continuous- and (d) pulse-flow operation. The color scheme in (i-iii) corresponds to the three colored dots located in the contour plots.

trigger additional side effects. For example, in the continuous-flow operation mode, concentration depletion is observed at the right bottom corner of negative electrode toward time instance T2 (Figure 10c). Ion starvation resulting from diffusion limitations inside porous electrodes was also observed in previous CDI models under constant voltage operation.⁵¹ Meanwhile, cell voltage rapidly approaches the voltage cutoff limit (Figure 10aiv), resulting in a decrease in the length of charge stage compared with pulse-flow operation.

Experimental comparison between pulse-flow and continuous operation.—To confirm the previous findings from numerical simulations, here we present experimental data obtained using a self-designed CDI cell to compare the desalination performance of pulse-flow operation and continuous-flow operation. Implementing the proposed pulse-flow operation in experiments requires in situ measurement of local concentration and a feed-back control algorithm. In lieu of that approach we performed simplified pulse-flow tests by setting the batch-time constant (see the Experimental setup and methods section). The flow rate in continuous operation was determined accordingly. The experimental results in Figure 11 showed a monotonic increase of SEC as current density increased from 3–20 A/m^2 . While these results indicate that pulse-flow operation has lower SEC than continuous-flow operation (after accounting for displacement), SEC deviates between the two cases by 37% and 9.3% at low and high current density, respectively. Furthermore, lower SEC in continuous-flow operation is expected if the dead-volume effects can be eliminated.

Conclusions

Conventional flow-by CDI suffers from a number of charge-efficiency loss mechanisms, including leakage current, co-ion repulsion, and residue of desalinated solution within electrodes and the flow channels. In this study, we have demonstrated that the commonly used continuous flow operation in CDI can lead to significant performance degradation at high current density if the temporal lag between the charge stage and desalination stage is not accounted for in the collection of effluent. To demonstrate this, we have used a porous

electrode model, which has been calibrated and validated based on a self-designed and fabricated flow cell. Simulations with this model reveal local regions of salt accumulation that are affected by the specific flow mode used. We showed that, without changing the system architecture, electrode composition, and operation metrics (i.e., operating voltage window, current density, and average flow rate), salt removal performance of a CDI system can be improved by using pulse-flow operation. Compared to traditional continuous-flow operation, simulation results showed that charge efficiency increased up to 23% at current density of 20 A/m^2 in pulse-flow operation, which leads to 73% decrease of specific energy consumption (kJ/mol-NaCl). In addition, the specific energy consumption and the degree of desalination predicted by the model of pulse-flow operation closely align with the predictions of the continuous operation model if the temporal lag between the charge and desalination stages (so-called displacement) is accounted for. Aside from its immediate application toward enhancing the performance of continuous-flow CDI, this finding

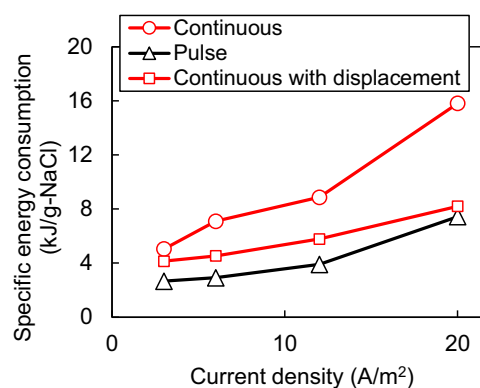


Figure 11. Experimental results of specific energy consumption for pulse-flow operation and continuous-flow operation at current densities ranging between 3–20 A/m^2 and with $C_0 = 30 \text{ mM}$.

suggests that one can approximate the performance in continuous-flow operation with predictions based on a one-dimensional pulse-flow model.

The present models incorporate the following non-ideal mechanisms in a CDI system: additional immobile surface charges on the positive electrode as a result of electrode degradation, leakage current due to different parasitic faradaic reactions on the positive and negative electrodes, repulsion of co-ions during electrosorption, and microscopic diffusive/advective salt transport. We also showed the experimental procedures and approaches necessary to extract the principle fittings parameters associated with different sub-modeling components. However, the model did not consider transport of minor ionic species such as H^+ and OH^- , which could play a role especially when faradaic reactions dominate utilization of current. With the addition of such effects within a porous electrode model, predicted charge efficiency and energy consumption for the various flow modes could be affected at low operating currents. In addition, future improvement to the model can be made by obtaining values for the PZC experimentally by measuring acidic and alkaline charge densities.

Acknowledgment

This work was funded by the US National Science Foundation Award No. 1605290 entitled "SusChEM: Increasing Access to Sustainable Freshwater Resources with Membrane Capacitive Deionization." Additional support for XS and KCS during the manuscript preparation process was from the Joint Center for Energy Storage Research, an Energy Innovation Hub funded by the U. S. Department of Energy, Office of Science, Basic Energy Sciences.

List of Symbols

a^*	effective surface area for faradaic reactions on porous electrode, m^2/cm^3 -electrode
c	electrolyte concentration, mM
$c_{ions,mi}$	ionic concentration in micropores, C/cm^3
C_S	Stern-layer capacitance, F/g
d_c	radius of a single activated particle, μm
D_0	bulk diffusion coefficient, cm^2/s
F	Faraday constant, C/mol
H_{O_2}	Henry's constant of oxygen, -
i_{0,O_2}	exchange current density for oxygen reduction, A/cm^2 -electrode
$i_{0,C}$	exchange current density for carbon corrosion, A/cm^2 -electrode
i_L	leakage current density, A/cm^3 -electrode
i_C	capacitive current density, A/cm^3 -electrode
I	total current applied to the system, A
k_B	Boltzmann constant, CV/K
N	number of pulses, -
Q_{pulse}	flow rate during the event of pulsing, mL/s
$\langle r_{mi} \rangle$	averaged radius of micropores, nm
t_-	transference number of negative ions, -
t_+	transference number of positive ions, -
T	temperature, K
$U_{O_2}^\theta$	standard potential of oxygen reduction, V vs. SHE
U_C^θ	standard potential of carbon corrosion, V vs. SHE
U_θ	Langmuir adsorption potential, V vs. SHE
V_{FC}	open volume in the flow channel, mL
V_{cell}	cell voltage, V
V_{pulse}	dispense volume during the event of pulsing, mL

Greek

α_{O_2}	symmetry factor for faradaic reaction of oxygen, -
α_C	symmetry factor for faradaic reaction of carbon, -
ϵ_{FC}	flow channel porosity, -

ϵ_{macro}	electrode porosity of macropores and voids between particles, -
ϵ_{micro}	electrode microporosity, -
ϵ	total electrode porosity, -
ϵ	computational error, -
η	overpotential for faradaic reactions, V
κ_0	bulk solution conductivity, S/m
κ_{eff}	effective conductivity in electrolyte, S/m
Δ_{FC}	charge efficiency loss due to desalination residue in flow channel, -
Δ_{co-ion}	charge efficiency loss due to co-ion repulsion, -
Δ_{ele}	charge efficiency loss due to desalination residue in electrodes, -
$\Delta_{leakage}$	charge efficiency loss due to leakage current, -
Δ_{salt}	charge efficiency due to salt removal in the effluent, or commonly referred to as charge efficiency, -
ϕ_e	solution-phase (electrolyte) potential, V
ϕ_s	solid-phase potential, V
$\Delta\phi_D$	Donnan layer potential or voltage drop across the boundary between micropore and macropore, V
$\Delta\phi_S$	voltage drop across the Stern layer, V
$\rho_{chem,i}$	fixed chemical charge density in micropores, C/cm^3
ρ_e	electric charge density, C/cm^3
$\rho_{electrode}$	electrode density, g/cm^3
$\rho_{mi,i}$	ionic charge density in micropores, C/cm^3
$\sigma_{s,eff}$	effective conductivity in solid phase, S/m

References

1. N. Ghaffour, T. M. Missimer, and G. L. Amy, *Desalination*, **309**, 197 (2013).
2. J. R. Ziolkowska and R. Reyes, *Applied Geography*, **71**, 115 (2016).
3. M. Suss, S. Porada, X. Sun, P. Biesheuvel, J. Yoon, and V. Presser, *Energy & Environmental Science*, **8**, 2296 (2015).
4. R. Zhao, S. Porada, P. Biesheuvel, and A. Van der Wal, *Desalination*, **330**, 35 (2013).
5. S. Porada, R. Zhao, A. Van Der Wal, V. Presser, and P. Biesheuvel, *Progress in Materials Science*, **58**, 1388 (2013).
6. A. M. Johnson and J. Newman, *Journal of the Electrochemical Society*, **118**, 510 (1971).
7. R. Zhao, P. Biesheuvel, and A. Van der Wal, *Energy & Environmental Science*, **5**, 9520 (2012).
8. R. Zhao, P. Biesheuvel, H. Miedema, H. Bruning, and A. Van der Wal, *The Journal of Physical Chemistry Letters*, **1**, 205 (2009).
9. I. Cohen, E. Avraham, Y. Bouhadana, A. Soffer, and D. Aurbach, *Electrochimica Acta*, **106**, 91 (2013).
10. D. He, C. E. Wong, W. Tang, P. Kovalsky, and T. D. Waite, *Environmental Science & Technology Letters*, **3**, 222 (2016).
11. M. He, K. Fic, E. Fra, P. Novák, and E. J. Berg, *Energy & Environmental Science*, (2016).
12. J. Dykstra, K. Keesman, P. Biesheuvel, and A. van der Wal, *Water Research*, **119**, 178 (2017).
13. P. Biesheuvel, H. Hamelers, and M. Suss, *Colloids and Interface Science Communications*, **9**, 1 (2015).
14. T. Wu, G. Wang, F. Zhan, Q. Dong, Q. Ren, J. Wang, and J. Qiu, *Water research*, **93**, 30 (2016).
15. S. Porada, L. Borchardt, M. Oschatz, M. Bryjak, J. Atchison, K. Keesman, S. Kaskel, P. Biesheuvel, and V. Presser, *Energy & Environmental Science*, **6**, 3700 (2013).
16. T. Kim and J. Yoon, *Journal of Electroanalytical Chemistry*, **704**, 169 (2013).
17. M. Zafra, P. Lavela, G. Rasines, C. Macías, J. Tirado, and C. Ania, *Electrochimica Acta*, **135**, 208 (2014).
18. M. E. Suss, T. F. Baumann, W. L. Bourcier, C. M. Spadaccini, K. A. Rose, J. G. Santiago, and M. Stadermann, *Energy & Environmental Science*, **5**, 9511 (2012).
19. Z. Peng, D. Zhang, T. Yan, J. Zhang, and L. Shi, *Applied Surface Science*, **282**, 965 (2013).
20. Y. Liu, T. Chen, T. Lu, Z. Sun, D. H. Chua, and L. Pan, *Electrochimica Acta*, **158**, 403 (2015).
21. H. Yin, S. Zhao, J. Wan, H. Tang, L. Chang, L. He, H. Zhao, Y. Gao, and Z. Tang, *Advanced materials*, **25**, 6270 (2013).
22. X. Xu, L. Pan, Y. Liu, T. Lu, Z. Sun, and D. H. Chua, *Scientific reports*, **5**, 8458 (2015).
23. S. Porada, L. Weinstein, R. Dash, A. Van Der Wal, M. Bryjak, Y. Gogotsi, and P. Biesheuvel, *ACS applied materials & interfaces*, **4**, 1194 (2012).
24. X. Gao, A. Omosebi, J. Landon, and K. Liu, *Energy & Environmental Science*, **8**, 897 (2015).
25. X. Gao, S. Porada, A. Omosebi, K. -L. Liu, P. Biesheuvel, and J. Landon, *Water research*, **92**, 275 (2016).
26. X. Gao, J. Landon, J. K. Neathery, and K. Liu, *Journal of The Electrochemical Society*, **160**, E106 (2013).

27. K. C. Smith and R. Dmello, *Journal of The Electrochemical Society*, **163**, A530 (2016).
28. P. Srimuk, J. Lee, S. Fleischmann, S. Choudhury, N. Jäckel, M. Zeiger, C. Kim, M. Aslan, and V. Presser, *Journal of Materials Chemistry A*, **5**, 15640 (2017).
29. J. Lee, S. Kim, C. Kim, and J. Yoon, *Energy & Environmental Science*, **7**, 3683 (2014).
30. S. Kim, H. Yoon, D. Shin, J. Lee, and J. Yoon, *Journal of Colloid and Interface Science*, **506**, 644 (2017).
31. S. Kim, J. Lee, C. Kim, and J. Yoon, *Electrochimica Acta*, **203**, 265 (2016).
32. J. P. Meyers and R. M. Darling, *Journal of the Electrochemical Society*, **153**, A1432 (2006).
33. H. Tang, Z. Qi, M. Ramani, and J. F. Elter, *Journal of Power Sources*, **158**, 1306 (2006).
34. J. -B. Lee, K. -K. Park, H. -M. Eum, and C. -W. Lee, *Desalination*, **196**, 125 (2006).
35. M. Haro, G. Rasines, C. Macias, and C. Ania, *Carbon*, **49**, 3723 (2011).
36. X. Gao, A. Omosebi, J. Landon, and K. Liu, *Environmental science & technology*, **49**, 10920 (2015).
37. E. Bayram and E. Ayranci, *Electrochimica Acta*, **56**, 2184 (2011).
38. X. Gao, A. Omosebi, J. Landon, and K. Liu, *Electrochemistry Communications*, **39**, 22 (2014).
39. K. B. Hatzell, E. Iwama, A. Ferris, B. Daffos, K. Urita, T. Tzedakis, F. Chauvet, P. -L. Taberna, Y. Gogotsi, and P. Simon, *Electrochemistry Communications*, **43**, 18 (2014).
40. T. Kim, J. Dykstra, S. Porada, A. Van Der Wal, J. Yoon, and P. Biesheuvel, *Journal of colloid and interface science*, **446**, 317 (2015).
41. C. Kim, J. Lee, P. Srimuk, M. Aslan, and V. Presser, *ChemSusChem*, (2017).
42. P. Srimuk, M. Zeiger, N. Jäckel, A. Tolosa, B. Krüner, S. Fleischmann, I. Grobelsek, M. Aslan, B. Shvartsev, and M. E. Suss, *Electrochimica Acta*, **224**, 314 (2017).
43. B. Shapira, I. Cohen, E. Avraham, and D. Aurbach, *Journal of The Electrochemical Society*, **164**, A1933 (2017).
44. A. Hemmatifar, J. W. Palko, M. Stadermann, and J. G. Santiago, *Water Research*, **104**, 303 (2016).
45. A. Omosebi, X. Gao, J. Landon, and K. Liu, *ACS applied materials & interfaces*, **6**, 12640 (2014).
46. T. Kim, J. Yu, C. Kim, and J. Yoon, *Journal of Electroanalytical Chemistry*, **776**, 101 (2016).
47. A. Hemmatifar, D. I. Oyarzun, J. W. Palko, S. A. Hawks, M. Stadermann, and J. G. Santiago, *Water Research*, (2017).
48. X. Gao, A. Omosebi, N. Holubowitch, A. Liu, K. Ruh, J. Landon, and K. Liu, *Desalination*, **399**, 16 (2016).
49. P. Biesheuvel, S. Porada, M. Levi, and M. Z. Bazant, *Journal of solid state electrochemistry*, **18**, 1365 (2014).
50. R. Zhao, O. Satpradit, H. Rijnaarts, P. Biesheuvel, and A. Van der Wal, *Water research*, **47**, 1941 (2013).
51. A. Hemmatifar, M. Stadermann, and J. G. Santiago, *The Journal of Physical Chemistry C*, **119**, 24681 (2015).
52. X. Gao, A. Omosebi, N. Holubowitch, J. Landon, and K. Liu, *Electrochimica Acta*, **233**, 249 (2017).
53. E. N. Guyes, A. N. Shocron, A. Simanovski, P. Biesheuvel, and M. E. Suss, *Desalination*, **415**, 8 (2017).
54. G. Doornbusch, J. Dykstra, P. Biesheuvel, and M. Suss, *Journal of Materials Chemistry A*, **4**, 3642 (2016).
55. H. Cohen, S. E. Eli, M. Jögi, and M. E. Suss, *ChemSusChem*, **9**, 3045 (2016).
56. K. C. Smith, Y. -M. Chiang, and W. C. Carter, *Journal of The Electrochemical Society*, **161**, A486 (2014).
57. M. Duduta, B. Ho, V. C. Wood, P. Limthongkul, V. E. Brunini, W. C. Carter, and Y. M. Chiang, *Advanced Energy Materials*, **1**, 511 (2011).
58. Z. Li, K. C. Smith, Y. Dong, N. Baram, F. Y. Fan, J. Xie, P. Limthongkul, W. C. Carter, and Y. -M. Chiang, *Physical Chemistry Chemical Physics*, **15**, 15833 (2013).
59. F. Y. Fan, W. H. Woodford, Z. Li, N. Baram, K. C. Smith, A. Helal, G. H. McKinley, W. C. Carter, and Y. -M. Chiang, *Nano letters*, **14**, 2210 (2014).
60. S. Sasi, A. Murali, S. V. Nair, A. S. Nair, and K. Subramanian, *Journal of Materials Chemistry A*, **3**, 2717 (2015).
61. Y. Qu, P. G. Campbell, L. Gu, J. M. Knipe, E. Dzenitis, J. G. Santiago, and M. Stadermann, *Desalination*, **400**, 18 (2016).
62. P. Biesheuvel and M. Bazant, *Physical review E*, **81**, 031502 (2010).
63. J. Newman and K. E. Thomas-Alyea, *Electrochemical systems*, John Wiley & Sons, 2012.
64. P. Biesheuvel, Y. Fu, and M. Z. Bazant, *Physical Review E*, **83**, 061507 (2011).
65. V. D. Bruggeman, *Annalen der physik*, **416**, 636 (1935).
66. P. Biesheuvel, *arXiv preprint arXiv:1509.06354* (2015).
67. P. Biesheuvel, M. Suss, and H. Hamelers, *arXiv preprint arXiv:1506.03948* (2015).
68. J. Chen, J. B. Siegel, T. Matsuura, and A. G. Stefanopoulou, *Journal of the Electrochemical Society*, **158**, B1164 (2011).
69. N. Takeuchi and T. F. Fuller, *Journal of The Electrochemical Society*, **155**, B770 (2008).
70. J. H. Ferziger and M. Peric, *Computational methods for fluid dynamics*, Springer Science & Business Media, 2012.
71. E. Protopapa, L. Ringstad, A. Aggeli, and A. Nelson, *Electrochimica Acta*, **55**, 3368 (2010).
72. B. Bradie, *A friendly introduction to numerical analysis: with C and MATLAB materials on website*, Prentice-Hall, 2006.
73. I. Cohen, E. Avraham, Y. Bouhadana, A. Soffer, and D. Aurbach, *Electrochimica Acta*, **153**, 106 (2015).
74. P. Długoteęcki and A. van der Wal, *Environmental science & technology*, **47**, 4904 (2013).
75. J. E. Dykstra, R. Zhao, P. M. Biesheuvel, and A. van der Wal, *Water research*, **88**, 358 (2016).